Spatiotemporal analysis of a final-state shape resonance in interferometric photoemission from Cu(111) surfaces

M. J. Ambrosio and U. Thumm
Physics Department, Kansas State University, Manhattan, Kansas 66506, USA

(Received 19 February 2019; published 21 October 2019)

Photoemission from solid targets includes the excitation and motion of electrons inside the substrate, followed by their propagation in vacuum and detection. It thus depends on the electronic band structure of the solid in the two distinct spectral domains of bound initial and continuum final states. While the imprint of the static (initial-state) valence electronic structure of solids on photoemission spectra is routinely examined in standard photoemission spectroscopy in the energy domain, state-of-the-art time-resolved photoelectron spectroscopy allows, in addition, the scrutiny of photoelectron propagation in the electronic continuum. Within a quantum-mechanical model for attosecond time-resolved interferometric photoelectron emission from solids, we calculated photoemission spectra as a function of the delay between the exciting primary attosecond pulse train and assisting infrared (IR) laser pulse. Accounting for final-state interactions of the photoelectron with the IR laser electric field and the periodic substrate, our numerical results for interferometric photoemission from the $3d$-valence band of Cu(111) surfaces show a striking resonantly enhanced sideband yield at photoelectron kinetic energies near 24 eV, in conjunction with a pronounced increase of the photoelectron wave-function amplitude inside the solid on a length scale of a few nanometers. This resonant shift of final-state photoelectron-probability density towards the bulk can be interpreted as an increase in the photoelectron propagation time in the solid and is commensurate with the resonantly enhanced spectral sideband-phase shifts observed in recent two-pathway two-photon interference spectra by Kasmi *et al.* [Optica **4**, 1492 (2017)].

DOI: 10.1103/PhysRevA.100.043412

I. INTRODUCTION

Tracking the spatiotemporal evolution of electronic motion in solids is of fundamental importance for basic and applied condensed matter physics and electrical engineering. The ability to monitor the dynamics of single electrons and collective electronic excitations at their natural time and length scales of a few attoseconds and less than one nanometer complements traditional energy-domain photoelectron spectroscopy carried out with long, quasi-continuum-wave pulses from synchrotron radiation sources [1].

Such time-domain investigations are enabled by the generation of higher-order harmonics (HHs) of intense femtosecond IR pulses in a noble-gas cell [2–4]. The HH pulse frequencies are equal to an odd multiple $(2n+1)$ of the IR-pulse frequency. Coherent superpositions of HH pulses emerge from the gas cell as a sequence of ultrashort pulses in the extreme ultraviolet (XUV) spectral range, referred to as attosecond pulse trains (APTs). APTs can be delayed relative to their driving IR pulse. The intensities of the IR pulse and APT are typically adjusted such that electrons are emitted by single-XUV-photon absorption and photoemission in the assisting IR pulse remains negligible. By focusing copropagating IR pulses and APTs on a target, photoemission spectra can be recorded as a function of the APT–IR-pulse delay (Fig. 1). These spectra show large photoelectron yields due to single-XUV-photon emission at photoelectron energies equal to the corresponding HH-photon energy minus the binding energy of the photoelectron initial state. We refer to this spectral feature as "HH yield" or "HH electrons." Due to the spectral composition of the APT, the kinetic energies of HH electrons differ by multiples of twice the IR-photon energy of the driving pulse.

Energetically located in between HH electrons, the photoemission spectra contain sidebands (SBs). A SB of order $2n$ (SB$2n$) is the result of the interference of ionization by a HH photon of order $2n-1$ and absorption of an IR photon with a second pathway, given by the ionization by a HH photon of order $2n+1$ and emission of an IR photon. A given SB$2n$ is energetically centered a single IR-photon energy below the energy of photoelectrons that are emitted after the absorption of a single HH photon of order $2n+1$ [HH$(2n+1)$]. It also lies a single IR-photon energy above photoelectrons that result from single-photon electron emission by a HH photon of order $2n-1$ [HH$(2n-1)$]. The SB-photoelectron yield oscillates with twice the frequency of the driving IR pulse as a function of the APT–IR-pulse delay. These SB oscillations are due to a two-photon two-pathway interference process, where both pathways result in equal photoelectron energies. Even though only the SBs involve interferometric photoemission, the delay-dependent spectra, including HH yields, are known as RABBITT (*reconstruction of attosecond beats by interference of two-photon transitions*) spectra. Temporal information, such as relative photoemission time delays, is retrieved from SB-yield oscillations in RABBITT spectra. The tracking of electronic dynamics in RABBITT spectra is thus based on the measurement of delay-dependent yield oscillations.

The RABBITT technique was first established for gas-phase targets [4–6]. It provides the same basic information on

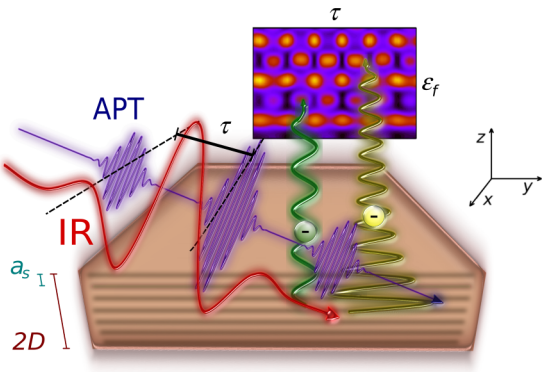

FIG. 1. Interferometric photoemission from a solid surface consists of single-XUV-photon absorption by two energetically adjacent high-order harmonics of the driving IR pulse, followed by either absorption or emission of an infrared photon. This leads to oscillating sideband yields at specific photoelectron kinetic energies ε_f as a function of the delay τ between the APT and IR pulse. At resonance, the amplitude of the final photoelectron wavefunction (associated with the right yellow photoelectron) is enhanced inside the solid in comparison to non-resonant emission (left green photoelectron). The resonant enhancement entails an observable characteristic increase in the interferometric sideband phase and, thus, in the spectral photoemission time delay.

the static electronic structure and dynamic electronic response of a target as the related streaking technique [7], where an isolated attosecond pulse replaces the APT. Two advantages of the RABBITT technique over streaked photoelectron spectroscopy are that (i) APTs are more conveniently produced in the laboratory than isolated attosecond pulses and (ii) RABBITT spectra typically require lower IR-pulse intensities (about 10^{11} W/cm^2), thus minimizing the perturbing influence of the IR pulse. These advantages are in part offset by unknown HH phases that need to be eliminated by comparison with a RABBITT reference spectrum [8]. This can be done by either simultaneously measuring SB phases for two different targets or by recording interferometric emission yields from energetically distinct initial states in the same target. An example for the first scheme for subtracting the unknown HH phases is the comparative measurement of RABBITT spectra from Ag(111) and Au(111) surfaces, using RABBITT spectra from gaseous argon by Locher *et al.* [9] as a reference. Examples for eliminating HH phases in RABBITT spectra of a single target are given by recording interferometric photoemission yields from energetically distinct bands in either Cu(111) or Ni(111) surfaces [10,11].

Currently, being well established for gaseous atomic targets [12–14], time-resolved photoelectron spectroscopy is rapidly expanding towards the investigation of the electronic structure of and dynamics in solids [8–11,15–24], adsorbate-covered surfaces [18,25], and nanoparticles [26,27]. Two recent interferometric photoemission experiments reveal strong, energetically localized, phase shifts in the delay-dependent SB-yield oscillations from Cu(111) [11,20] and Ni(111) [10,11] surfaces. These phase enhancements were interpreted as final-state resonances in the transition-metal periodic potentials and related to the (non-free-electron) dispersive propagation of the photoelectron. In the RABBITT experiment of Kasmi *et al.* [20] the Cu(111) surface was oriented such that the photoelectron image of the 3*d*-valence band splits into two easily distinguishable subbands. For each 3*d* subband, a spectral SB phase could be extracted from the RABBITT spectra that showed a pronounced, resonance-like increase at SB20, corresponding to final photoelectron kinetic energies of $\varepsilon_f \approx 24$ eV. Similar final-state resonance effects were observed in time-resolved interferometric photoemission experiments from Ni(111) surfaces by Tao *et al.* [10] and from Cu(111) and Ni(111) surfaces by Chen *et al.* [11].

We here extend our previous investigation of interferometric photoemission from transition-metal surfaces [24] by refining the modeling of the final photoelectron state in our quantum-mechanical calculation of interfering photoemission amplitudes. We employ a semiclassical representation of the final photoelectron state that includes interactions of the active electron with the IR laser and periodic substrate. We apply our model to interferometric photoemission from a Cu(111) surface and discuss numerically calculated RABBITT spectra and SB phases for the photoelectron-emission geometry and APT- and IR-pulse parameters of Ref. [20]. By carefully adjusting the initial valance states to experimental APT-only spectra given in the Supplemental Material of Ref. [20], our calculation is able to reproduce the experimentally observed final-state resonance.

Scrutinizing the spatial dependence of resonant and non-resonant final states predicted by our model offers an intuitive explanation for the measured resonant SB-phase change in terms of a resonant shift of final-state probability density away from the metal-vacuum interface towards the interior of the substrate. For the employed APT parameters, the photoelectron-escape depth is limited by the finite photoelectron mean-free path to a few layer spacings of the crystalline substrate. Nevertheless, the probability-density shift away from the interface strongly affects the photoelectron yield and energy-dependent SB phases, highlighting the nm-scale sensitivity of interferometric electron emission from metal surfaces.

The work of Kasmi *et al.* [20] includes a comparison their of experimental results with a hybrid model for ballistic electron transport. This model relates the electron-transport time to the energy-dependent photoelectron mean-free path in the solid and the photoelectron group velocity. In the analysis of their experimental data, the authors show, that assuming free-electron-like final states (i.e., free-electron dispersion in the solid), this model fails to match the measured pronounced increase in the photoemission delay near final photoelectron energies of 24 eV. In contrast, employing photoelectron group velocities based on density-functional-theory (DFT) calculations and a weighted sum of quantum-mechanically approximated photoemission probabilities, the authors' model predicts a resonance-like delay increase near 18.5 eV. This finding is consistent with a significant influence of the substrate band structure on the photoelectron escape velocity and photoemission delay.

The transport model of Kasmi *et al.* [20] elucidates the measurable effect of non-free electron dispersion during photoemission. However, its hybrid nature and underlying classical assumption of the total photoelectron transport time as the

ratio of the photoelectron mean-free path and group velocity warrant additional scrutiny. The quantum-mechanical model presented here further examines the influence of the substrate on the propagation of the released photoelectron inside and outside the solid. In contrast to the model developed by Kasmi *et al.*, our calculation is based on the direct evaluation of the quantum-mechanical transition amplitude and a heuristic generalization of well-known Volkov states for the propagation of electrons in homogeneous electromagnetic fields. While confirming the main conclusion reached by Kasmi *et al.* of relevant final-state electron-substrate interactions, our analysis permits the interpretation of the observed photoemission-delay increase as a purely quantum-mechanical final-state shape resonance in the semiperiodic substrate potential.

We organized this paper as follows. In Sec. II we describe our quantum-mechanical model with emphasis on our representation of the initial $3d$-valence-band electronic states (Sec. II A) and our semiclassical modeling of the photoelectron final states in terms of generalized Volkov states for the motion of an electron in a continuum-wave electric field (Sec. II B). Section III contains our numerical results for interferometric photoemission from a Cu(111) surface. Section III A describes how we adjust the initial-state parameters to reproduce the APT-only spectra measured in Ref. [20]. Section III B characterizes and illustrates the spatial distribution of resonant and nonresonant final photoelectron states. Calculated RABBITT spectra for different final-state models are discussed in Sec. III C. The corresponding SB-phase shifts are compared in Sec. III D with the experimental phases of Ref. [20]. A summary and outlook are given in Sec. IV, followed by three appendices that include details of an approximate analytical final-state model. Throughout this work we use atomic units and set the electronic energy scale to zero at the ionization threshold, unless otherwise specified.

II. THEORY

We assume photoemission by a single XUV photon of the APT. This assumption is justified since emission by two or more XUV photons leads to distinguishable final photoelectron energies that do not overlap with the single-XUV-photon emission spectrum. In addition, emission by two or more XUV photons is much less likely to occur than single-photon emission for the considered XUV intensities. The probability per unit surface area for photoemission of electrons into the solid angle $\Delta\Omega_f$ with final, detectable momentum $\mathbf{k}_f$ as a function of the time delay τ between the centers of the APT and assisting IR pulse is given by

$$P(\varepsilon_f,\tau)=\sqrt{2\varepsilon_f}\int_{\Delta\Omega_f}d\Omega_f\sum_{|\mathbf{k}_i|<k_F}\left|T_{\mathbf{k}_f,\mathbf{k}_i}(\tau)\right|^2. \tag{1}$$

This expression includes the incoherent superposition of all occupied initial conduction-band states of the target surface with momenta $\mathbf{k}_i$ of magnitudes k_i smaller than the Fermi momentum k_F. We calculate the transition amplitude between initial states $\Psi^i_{\mathbf{k}_i}$ and final states $\Psi^f_{\mathbf{k}_f}$ in the velocity gauge and without resorting to the dipole approximation in terms of the transition matrix

$$T_{\mathbf{k}_f,\mathbf{k}_i}(\tau)\propto\int_{-\infty}^{\infty}dt\left\langle\Psi^f_{\mathbf{k}_f}(\mathbf{r},t,\tau)\middle|\mathbf{A}_{\mathrm{XUV}}(\mathbf{r},t)\cdot\nabla\middle|\Psi^i_{\mathbf{k}_i}(\mathbf{r},t)\right\rangle. \tag{2}$$

With the bracket $\langle\cdots\rangle$ we refer to the spatial integration over the Cartesian components x, y, and z of the electron position vector $\mathbf{r}$. The vector potential of the spatially inhomogeneous APT,

$$\mathbf{A}_{\mathrm{XUV}}(\mathbf{r},t)=\sum_n\mathbf{A}^{2n+1}_{\mathrm{XUV}}(\mathbf{r},t), \tag{3a}$$

$$\mathbf{A}^{2n+1}_{\mathrm{XUV}}(\mathbf{r},t)=\mathbf{a}^{2n+1}_{\mathrm{XUV}}e^{-\alpha_{2n+1}t^2+i(\mathbf{k}_{2n+1}\cdot\mathbf{r}-\omega_{2n+1}t+\phi^{\mathrm{HH}}_{2n+1})}, \tag{3b}$$

is defined by the superposition of odd HHs of the IR-pulse frequency ω_{IR} with frequencies $\omega_{2n+1}=(2n+1)\omega_{\mathrm{IR}}$, Gaussian temporal profiles of full widths at half intensity maximum (FWHIM) $\sqrt{\ln 2/(2\alpha_{2n+1})}$, photon momenta $\mathbf{k}_{2n+1}$, and phase offsets $\phi^{\mathrm{HH}}_{2n+1}$. The amplitudes $\mathbf{a}^{2n+1}_{\mathrm{XUV}}$ are deduced from the peak intensities in Fig. S1(b) in the Supplemental Material of Ref. [20].

In our numerical applications, we adopt the pulse-incidence and electron-detection geometry, as well as the APT- and IR-pulse parameters, of Ref. [20]. Accordingly, we assume an XUV APT consisting of odd high-harmonics $2n+1=15$ through 25 with equal spectral widths of 0.2 eV (FWHIM) (extracted from Fig. S1(b) in the Supplemental Material of Ref. [20]), an IR-pulse peak intensity of 2.0×10^{11} W/cm^2, and an IR-pulse width of 25 fs (FWHIM). For the considered range of kinetic energies, the energy-dependent inelastic mean-free paths lie between 10 and 25 a.u. [28]. The photoelectron escape depth is thus limited to a few interlayer spacings, $a_s=3.94$ a.u., of Cu(111) [29]. The XUV skin depth is larger than 200 a.u. [30], and thus by far exceeds the escape depth. We therefore disregard diffraction and attenuation of the APT inside the solid. We include the interaction of the photoelectron with the assisting IR pulse in the final state as detailed in Sec. II B below.

A. Initial state

By rotating the surface orientation, Kasmi *et al.* [20] selected an emission geometry for which interferometric photoemission spectra map the $3d$-valence band of Cu(111) into two distinguishable narrow subbands. Adhering to the designation by the authors, we refer to these bands with respect to their binding energies as lower (L) and upper (U) bands. We represent both subbands by their narrow-band limits and extracted the central sub-band energies $\varepsilon^{(L)}_{\mathrm{bnd}}=-7.94$ eV and $\varepsilon^{(U)}_{\mathrm{bnd}}=-7.17$ eV, respectively, from the experimental spectra given in Fig. S8 in the Supplemental Material of Ref. [20]. We adopt the Fermi energy $\varepsilon_F=4.92$ eV [31].

For our numerical evaluation of the photoemission yield (1), we assume a translationally invariant surface. We model the initial $3d$-valence-band wave functions in the single-active-electron approximation as

$$\Psi^i_{\mathbf{k}_i}(\mathbf{r},t)=e^{i\mathbf{k}_{i,\parallel}\cdot\mathbf{r}_\parallel}\chi_{k_{i,z}}(z)e^{-i\varepsilon_{\mathrm{bnd}}t}, \tag{4}$$

with binding energies $\varepsilon_{\rm bnd} = \varepsilon_{\rm bnd}^{(U,L)}$. We expand the surface-normal component,

$$\chi_{k_{i,z}}(z) = \sum_j e^{ik_{iz}z_j}\varphi(\varepsilon_H, \alpha_H, n_H, |z - z_j|), \tag{5}$$

of the initial wave function in a basis of Hulthén generalized Sturmian functions (GSFs) φ [32–34], representing the interaction between the active $3d$-band electron with the screened Coulomb field of atomic cores. The GSFs are localized at the crystal-lattice-plane positions $z = z_j$ along the surface-normal (z) direction.

We separately calculate photoemission spectra for the U and L bands in the narrow-bandwidth limit by setting the GSF energies $\varepsilon_H = \varepsilon_{\rm bnd}^{(L)}$ and $\varepsilon_H = \varepsilon_{\rm bnd}^{(U)}$, respectively. The GSF parameters n_H and α_H specify the number and distribution of the wave-function nodes of φ, respectively. We determined these parameters to obtain the best agreement between the XUV-only spectrum shown in Fig. S7 in the Supplemental Material of Ref. [20], and numerical calculations we carried out for vanishing IR-field strength. The $3d$ band of Cu(111) includes states with electron-orbital-angular-momentum projections $|m| \leqslant 2$ along the surface normal which, in full dimensionality, would be accounted for by the phase factor $e^{im\phi}$, where $\tan\phi = y/x$. Since, for a translationally invariant surface, only $m = 0$ orbitals contribute in the average over the surface (x, y) plane, we only include GSFs with positive $z \to -z$ parity.

B. Final state

We construct the final continuum state of the photoelectron as a modified Volkov wave function,

$$\Psi_{\mathbf{k}_f}^f(\mathbf{r}, t, \tau) \propto f_{\varepsilon_f,\theta_f}(z) e^{i\mathbf{k}_{f,\parallel}\cdot\mathbf{r}_\parallel} \psi_{k_{f,z}}(z) e^{i\phi_{\mathbf{k}_f}(z,t_d)} e^{-i\varepsilon_f t}, \tag{6}$$

where $\psi_{k_f}(z)$ is the final wave-function Cartesian component along the surface normal. The assumed translational invariance of the final state in the surface plane is expressed by the plane-wave factor with momentum $\mathbf{k}_{f,\parallel}$. Volkov wave functions, originally introduced as exact quantum-mechanical solutions for the motion of an electron in an infinitely extended (continuum-wave) homogeneous external field [35], account for the interaction with the external field in the Volkov phase $\phi_{\mathbf{k}_f}$. The asymptotic photoelectron momentum $\mathbf{k}_f$ is oriented at the angle θ_f relative to the surface normal, and the observable final photoelectron energy is given by the free-electron-dispersion relation $\varepsilon_f = k_f^2/2$. The final energy associated with the photoelectron motion along the surface-normal direction is thus $\varepsilon_{f,z} = \varepsilon_f \cos^2\theta_f$. The damping function

$$f_{\varepsilon_f,\theta_f}(z) = \Theta(z) + e^{z/[2\lambda(\varepsilon_f)\cos(\theta_f)]}\Theta(-z) \tag{7}$$

accounts for photoemission-yield losses (electrons not reaching the detector) due to collisions in the substrate. It limits relevant contributions to photoemission to a few energy-dependent mean-free paths $\lambda(\varepsilon_f)$. For the XUV energies considered in this work this escape depth amounts to a few surface layers. $\Theta(z)$ denotes the Heaviside unit-step function. For our numerical computations we adopt the calculated mean-free-path values of Ref. [28].

1. Semiclassically generalized Volkov phase for spatially inhomogeneous IR fields

The electric field of the incident assisting IR pulse is spatially *inhomogeneous* near the conducting Cu(111) surface, due to superposition with its Fresnel-reflected pulse [19] and strong absorption inside the solid over a length of a few interlayer spacings [18]. The time-dependent DFT calculation in Ref. [18] suggests that screening starts at approximately half an interlayer spacing outside the topmost layer at $z = 0$. Accordingly, we assume complete screening of the incident IR pulse at the image plane $z = z_{im}$,

$$\mathbf{E}_{\rm IR}(z, t) = \begin{cases} \mathbf{E}_{\rm IR}^{\rm out}(t), & z \geqslant z_{im}, \\ 0, & z < z_{im}, \end{cases} \tag{8}$$

and approximate the superposition of the incident and reflected IR pulse near the surface by the *homogenous* field $\mathbf{E}_{\rm IR}^{\rm out}(t)$ [9,19]. The assumption of a homogeneous Fresnel-reflected IR electric field outside the substrate is justified by noticeable contributions to the transition amplitude (2) from outside the surface being cut off by the rapid exponential decay of the initial-state wave-function amplitude over a range of electron-surface distances z that are much smaller than the IR wavelength (≈800 nm).

According to Eq. (8) the XUV-excited photoelectron needs to propagate to the optical surface at $z = z_{im}$ before becoming exposed to the IR field. In modeling the photoelectron interaction with the IR-laser field (8), we generalize the original Volkov phase [35] by accounting classically for photoelectron transport along trajectories $\tilde{z}(z, t')$ that start at z at time t:

$$\phi_{\mathbf{k}_f}(z, t_d) = \mathbf{k}_f \cdot \int_t^\infty dt'\, \mathbf{A}_{\rm IR}[\tilde{z}(z, t'), t'_d]. \tag{9}$$

The definitions $t_d = t - \tau$ and $t'_d = t' - \tau$ imply that the delay τ is positive (negative) if the center of the APT leads (trails) the IR pulse. We evaluate the vector potential from the electric field,

$$\mathbf{A}_{\rm IR}(\tilde{z}, t_d) = \int_t^\infty dt'\, \mathbf{E}_{\rm IR}(\tilde{z}, t'_d) \approx \int_{t_{\rm surf}(z_j)}^\infty dt'\, \mathbf{E}_{\rm IR}^{\rm out}(t'_d), \tag{10}$$

taking advantage of Eq. (8). Next, we exploit the localization of the GSFs at $z = z_j$ to approximate the propagation phase for photoelectrons that are released from atomic layers at $z = z_j$ as $\phi_{\mathbf{k}_f}(z, t_d) \approx \phi_{\mathbf{k}_f}(z_j, t_d)$. This approximation amounts to calculating $\phi_{\mathbf{k}_f}(z, t_d)$ for piecewise homogeneous electric fields. For the IR intensity considered in our numerical calculation and in Ref. [20], the ponderomotive phase shift ($\propto A_{\rm IR}^2$) can be neglected in Eq. (9). The time integration in Eq. (10) effectively starts at the instant $t_{\rm surf} = t + t_{\rm transp}$, when the photoelectron reaches the optical surface at $z = z_{im}$. The transport time for the ballistic propagation of the photoelectron between its release at $z = z_j$ and its arrival at $z = z_{im}$ is $t_{\rm transp} = (z_{im} - z_j)/k_z$. The assumption of a constant momentum k_z during the propagation of the photoelectron in the solid is justified by the analytical considerations in Appendix A and the numerical results in Sec. III B 2 below.

2. Substrate electronic structure and photoemission boundary conditions

We model the influence of the crystalline substrate on $\psi_{k_{f,z}}$ in terms of a z-dependent model potential for a slab of width $2D$, following the parametrization of DFT-calculated numerical electronic potentials for periodic substrates introduced by Chulkov [29,36]:

$$V_C(z') = \begin{cases} A_0 \frac{\exp[-\lambda_C(z'-z_{im})]-1}{4(z'-z_{im})}, & z_{im} < z', \\ A_3 \exp[-\alpha_C(z'-z_1)], & z_1 < z' < z_{im}, \\ -A_{20} + A_2 \cos[\beta(z'-D)], & D < z' < z_1, \\ A_{10} + A_1 \cos\left(\frac{2\pi}{a_s} z'\right), & 0 < z' < D. \end{cases} \tag{11}$$

Here, $V_C(z') = V_C(-z')$, $z' = z + D$, and $D = n_D\, a_s$, where n_D is the number of layers. The topmost atomic layer is centered at $z = 0$ ($z' = D$) [cf. Fig. 3(d) below]. The limit of a semi-infinite substrate is reached for $D \to \infty$. This model potential accounts for two important physical attributes of the photoelectron wave packets: their propagation in the substrate subject to a lattice-periodically changing effective force and kinetic-energy loss upon emission from the surface. Potentials of the form (11) have been extensively used to model electron–metal-surface interactions [8,17,37–41]. These calculations are performed after adjusting the set of independent parameters A_{10}, A_1, A_2, and β to the main characteristics of the substrate valence electronic structure (energetic location of the band-gap, surface-state, and image-states energies) predicted either by calculations [42,43] or by photoemission experiments [44,45]. The dependent parameters, A_{20}, A_3, α_C, λ_C, z_1, and z_{im} are determined by imposing the continuity of the potential and its derivative at the matching points $|z'| = D$, z_1, and z_{im}.

The independent parameter values A_{10}, A_1, A_2, and β for Cu(111) reported in Ref. [29] are -11.895 eV, 5.14 eV, 4.3279 a.u., and 2.9416 a.u., respectively. By setting in Eq. (11) $A_0 = 27.211$ eV, we obtain $V_C(z)$ in units of eV. In our numerical applications in Sec. III below, the only model parameters we readjust are the oscillation amplitude A_1 and the bulk-potential depth A_{10}. Details for this readjustment are given in Sec. III B. It allows us to imprint the substrate electronic structure on outgoing photoelectron wave packets so that our calculated spectra reproduce the measured interferometric photoemission spectra and photoemission delays in Ref. [20].

The surface-normal component $\psi_{k_{f,z}}$ of the final photoelectron wave function is subject to outgoing-wave boundary conditions at large distances $z \to \infty$ from the surface. Based on the parameterized potential (11), we numerically calculated $\psi_{k_{f,z}}$ exactly by Numerov propagation [46], imposing outgoing-wave boundary conditions. To assess the effect of wave-function reflections inherent in the exact solution on interferometric photoemission spectra, we also determined $\psi_{k_{f,z}}$ based on a Wentzel-Kramers-Brillouin (WKB) approximation [46,47], denoted as $\psi^{\mathrm{WKB},1}_{k_{f,z}}$, that does not include the reflection of the outgoing photocurrent in the corrugated potential V_C (see Appendix A).

3. Approximated transition amplitude

Under the assumptions made in Sec. II B above, the transition amplitude (2) can be approximated by the expression

$$\begin{aligned} T_{\mathbf{k}_f,\mathbf{k}_i}(\tau) \propto \sum_n \sum_j e^{ik_{iz}z_j} \int_{-\infty}^{\infty} dt\, e^{i(\varepsilon_f - \varepsilon_{\mathrm{bnd}})t} \\ \times \left\langle f_{\varepsilon_f,\theta_f}(z) e^{i\mathbf{k}_{f,\parallel}\cdot\mathbf{r}_\parallel} \psi_{k_{f,z}}(z) e^{i\phi_{\mathbf{k}_f}(z_j,t_d)} \left| \mathbf{A}^{2n+1}_{\mathrm{XUV}}(\mathbf{r},t)\cdot\nabla \right. \right. \\ \times \left. \left| e^{i\mathbf{k}_{i,\parallel}\cdot\mathbf{r}_\parallel} \varphi(\varepsilon_H, \alpha_H, n_H, |z - z_j|) \right\rangle \right\rangle, \end{aligned} \tag{12}$$

which we evaluate numerically.

III. NUMERICAL RESULTS

We arranged this section as follows. In Sec. III A we discuss our adjustment of the initial-state wave-function parameters α_H and n_H in Eq. (4) and of the screening parameter ζ (defined in Sec. III A) to best reproduce the measured XUV-APT-only spectrum in Ref. [20]. Next, in Sec. III B, we carefully analyze the properties of the final photoelectron state (6) with particular emphasis on its distinctive role in accounting for the resonant photoelectron dynamics observed in recent interferometric photoemission experiment by Kasmi *et al.* [20]. Finally, in Secs. III C and III D, we present simulated interferometric (RABBITT) spectra and corresponding phases, respectively, and compare our simulation results with the RABBITT phases deduced from measured spectra in Ref. [20], again with focus on final-state-resonance effects.

The general idea behind our determination of initial- and final-state parameters is to tune n_H, α_H, and ζ to match the XUV-APT-only spectrum in Ref. [20] and to adjust the parameters A_1 and A_{10} in the substrate potential V_C in Eq. (11) to the RABBITT spectra in Ref. [20]. We note, however, that the fitting of initial- and final-state parameters to measured photoelectron spectra cannot be performed completely separately, since the calculated photoemission probability depends on all parameters. To adjust the wave-function parameters in our numerical RABBITT spectra compared in Secs. III C and III D below with the measured spectra of Ref. [20] we proceeded as follows:

(i) We first performed trial calculations with the parameter values $n_H = 3$, $\alpha_H = 0.2a_s$. We selected these values close to the parameter values in our previous simulations of RABBITT spectra from Ag(111) and Au(111) surfaces [24]. For these start values, we adjusted the parameters A_1 and A_{10} to best reproduce the experimental RABBITT spectra and phases in Ref. [20]. In this first round of parameter adjustments we obtained $A_1 = 13.0$ eV and $A_{10} = -16.58$ eV.

(ii) Next, we kept these values for A_1 and A_{10} fixed and adjusted α_H, n_H, and ζ to match the XUV-APT-only spectrum in Ref. [20], as described in Sec. III A. This results in $\alpha_H = 0.25a_s$ and $n_H = 5$.

(iii) In the final round of parameter adjustments, we kept the values for α_H, n_H, and ζ from (ii) and readjusted the parameter A_1 to best reproduce the experimental RABBITT spectra and phases in Ref. [20]. The final value we obtained is $A_1 = 13.52$ eV.

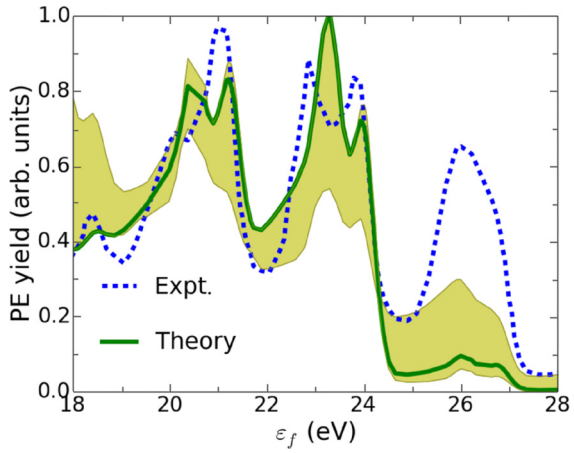

FIG. 2. Background-corrected calculated (green solid curve) in comparison with the measured APT-XUV-only spectrum of Ref. [20] (blue dotted curve). The calculated results were obtained for the parameter values $n_H = 5$, $\alpha_H = 0.25a_s$, and $\zeta = 1.7$. The light green shaded area indicates the variation of our calculated photoelectron yield for $\alpha_H \in [0.1, 0.4] \times a_s$ and $\zeta \in [0.5, 2.0]$.

A. Initial-state optimization

We adjusted the nodal-structure parameters n_H and α_H of the GSFs (5) in the initial state (4) by least-squares optimizing the agreement between our calculated and the measured XUV-APT-only spectrum published in the Supplemental Material of Ref. [20]. For this purpose, we numerically evaluated Eqs. (1) and (12) after (i) setting the IR electric field $\mathbf{E}_{\mathrm{IR}}^{\mathrm{out}}$ in Eq. (8) equal to zero and (ii) adding a background of secondary electrons to our calculated spectrum. We approximated the secondary-electron-background contribution in the measured spectrum by accounting for photoelectron-energy loss due to elastic collisions with other electrons, representing electron-electron interactions in terms of a screened Coulomb-interaction potential ($\propto e^{-r/\zeta}/r$). Details of this background-subtraction model can be found in Ref. [24].

In order to find the best fit of our background-corrected simulation to the measured APT-XUV-only spectrum, we performed calculations for different parameters $n_H \in [1, 6]$ and $\alpha_H \in [0.1, 0.4] \times a_s$. Subsequently, for each pair of parameters n_H and α_H, we least-squares fitted a linear combination of our simulated background-corrected APT-XUV-only photoelectron yield, allowing for screening lengths ζ between 0.5 and 2.0 a.u.. This fitting protocol leads to the best agreement with the measured APT-XUV-only spectrum for $n_H = 5$, $\alpha_H = 0.25a_s$, and the screening parameter $\zeta = 1.7$ a.u. (Fig. 2). Among the adjustable parameters of the substrate model potential (11), the oscillation amplitude A_1 most strongly affects the RABBITT phases at the resonant energy. We obtained the quoted values for n_H, α_H, and ζ in conjunction with the bulk-potential-oscillation amplitude $A_1 = 13.0$ eV and potential depth $A_{10} = -16.58$ eV. This value for A_1 produced the best agreement of the measured and calculated RABBITT phases in a series of preliminary calculations we carried out before the initial-state optimization.

B. Final-state wave function

In this subsection we analyze the properties of the final state $\psi_{k_{f,z}}$ in both, its coordinate-space representation in Eq. (6) and in momentum space. In order to examine the resonant behavior of the interferometric photoemission process, we compare the exact numerical solution for $\psi_{k_{f,z}}(z)$ with the approximate first-order WKB solution $\psi_{k_{f,z}}^{\mathrm{WKB},1}(z)$. Details of the derivation of $\psi_{k_{f,z}}^{\mathrm{WKB},1}(z)$ are given in Appendix A. While both the exact and approximated final states satisfy outgoing-wave boundary conditions, the approximate WKB-type solution lacks reflections of the quantum-mechanical current inside the substrate near the lattice planes of the oscillating model potential V_C (11). Superpositions of contributions to the final state that are incident and reflected in the periodic force field of the substrate are prerequisite for the formation of final-state resonances. The comparison of spectra calculated with $\psi_{k_{f,z}}(z)$ (including final-state resonance effects) and $\psi_{k_{f,z}}^{\mathrm{WKB},1}(z)$ therefore allows us to interpret the resonance behavior observed in the interferometric spectra in Ref. [20] as a resonance phenomenon imposed by the dispersive photoelectron propagation in the solid. To *analytically* reveal distinct properties of the final photoelectron state imposed by the periodic substrate potential, we further approximate $\psi_{k_{f,z}}(z)$ by a zeroth-order WKB-type wave function $\psi_{k_{f,z}}^{\mathrm{WKB},0}(z)$, the mathematical derivation of which is contained in Appendices A and C.

1. Coordinate-space analysis

We model the final-state wave function $\psi_{k_{f,z}}(z)$ as a continuum state in the substrate potential V_C in Eq. (11) that satisfies outgoing-wave boundary conditions at large z. With the specific parametrization of V_C given in Ref. [29] for Cu(111) surfaces, we calculated both exact continuum eigenstates $\psi_{k_{f,z}}(z)$ and approximate solutions $\psi_{k_{f,z}}^{\mathrm{WKB},1}(z)$ as a function of their corresponding energy eigenvalues $\varepsilon_{f,z}$ by numerical Numerov propagation of the time-independent Schrödinger-equation [46] for the potential-depth parameter $A_{10} = -11.895$ eV of Ref. [29]. Our numerical results in Fig. 4 show a strong enhancement of the maximal wave-function amplitude $|\psi_{k_{f,z}}(z)|$ for $z \in [-100, 0]$ a.u. at the energy $\varepsilon_{f,z}^{\mathrm{res}} = 23.94$ eV (We add the superscript "res" to reflect the resonant behavior of the energy-dependent final-state wave-function). This amplitude enhancement depends on the wave-function-oscillation amplitude A_1 in Eq. (11) and is less pronounced for the value $A_1 = 5.14$ eV given in Ref. [29] than for $A_1 = 7.71$ eV.

Figure 3 shows the real parts of the exact final-state wave function $\psi_{k_{f,z}}(z)$ and of the approximate solution $\psi_{k_{f,z}}^{\mathrm{WKB},1}(z)$ at the resonance energy $\varepsilon_{f,z}^{\mathrm{res}} = 23.94$ eV (solid green lines) and for the nonresonant final-state energy $\varepsilon_{f,z} = 28.22$ eV (blue dotted lines). The position dependences of $\psi_{k_{f,z}}(z)$ for the value $A_1 = 5.14$ eV given in Ref. [29] in Fig. 3(a) and for $A_1 = 7.71$ eV in Fig. 3(b) differ dramatically. As shown in Fig. 3(b), at the resonance energy $\varepsilon_{f,z}^{\mathrm{res}}$ this 1.5-fold increase of A_1 entails a strong increase of the wave-function amplitude inside the substrate (towards negative z values), starting at the surface layer ($z = 0$). As illustrated in Fig. 3(b), this net displacement of electronic probability density away from the

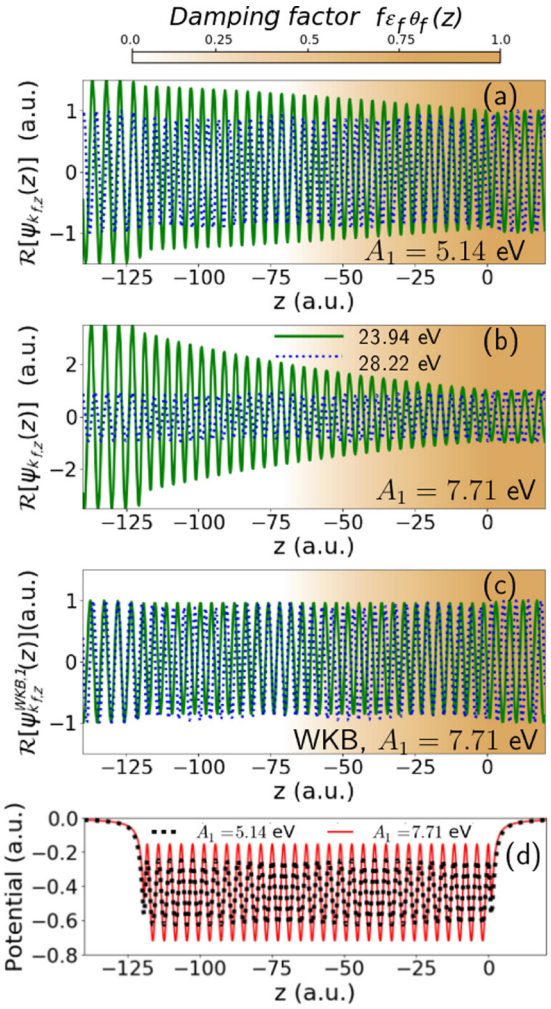

FIG. 3. (a)–(c) Real part of the final photoelectron wave function for a Cu(111) slab of thickness $2D = 120$ a.u. at the resonance energy $\varepsilon^{\rm res}_{f,z} = 23.94$ eV (solid green line) and at $\varepsilon_{f,z} = 28.22$ eV (dotted blue line). The values of the bulk-potential-oscillation amplitude are (a) $A_1 = 5.14$ eV and (b,c) 7.71 eV. (c) Amplitude of the approximate WKB-type wavefunction $\psi^{\rm WKB,1}_{k_{f,z}}(z)$ that excludes reflections of the outgoing electron in the periodic substrate potential. The orange/gray shade illustrates the decreasing photoelectron-escape probability due to the finite photoelectron mean-free path. (d) Chulkov potential $V_C(z)$ according to Eq. (11) of a 120 a.u. thick slab for the values of A_1 in (a)–(c).

surface towards the bulk occurs only at the resonance energy $\varepsilon^{\rm res}_{f,z}$ and is absent off resonance, at $\varepsilon_{f,z} = 28.22$ eV. We will thus refer to this significant increase of the final-state wavefunction amplitude in the substrate as "resonance."

The resonance enhancement observed in the exact final-state wave function at $\varepsilon^{\rm res}_{f,z} = 23.94$ eV and $A_1 = 7.71$ eV in Fig. 3(b) is absent in the approximate wave function $\psi^{\rm WKB,1}_{k_{f,z}}(z)$, due to suppressed wave-function reflections within the substrate [Fig. 3(c)]. The absence of resonant amplitude enhancement at $\varepsilon^{\rm res}_{f,z}$ in Fig. 3(c) lends additional support to the interpretation of the numerically observed shift in the probability density towards the bulk side of the surface as a resonance effect. Off resonance, at the higher energy $\varepsilon_{f,z} = 28.22$ eV, neither the wave function $\psi_{k_{f,z}}(z)$

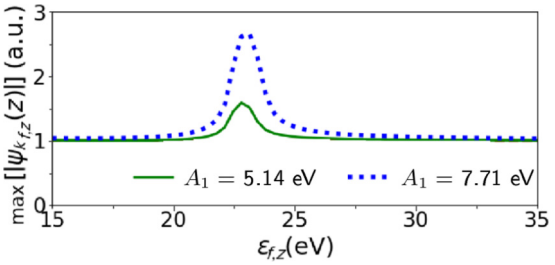

FIG. 4. Maximal final-state wave-function amplitude $\max(|\psi_{k_{f,z}}(z)|)$ for $z \in [-100, 0]$ a.u. as a function of the energy $\varepsilon_{f,z}$, for the two values of the bulk-potential-oscillation amplitudes A_1 in Fig. 3.

nor the approximation $\psi^{\rm WKB,1}_{k_{f,z}}(z)$ show a noticeable amplitude increase inside the solid [Figs. 3(a)–3(c)]. We will demonstrate in Secs. III C and III D below that the resonant final-state probability-density enhancement in the solid puts increased weight on electron emission from deeper layers. This results (in the quantum-mechanical average) in increased photoelectron-transport times and, thus, in larger RABBITT phase shifts.

For the two values of A_1 applied in Figs. 3 and 4, the change in resonance energy is small and irrelevant for the discussion of these figures. We continue to examine the weak dependence of $\varepsilon^{\rm res}_{f,z}$ on A_1 in Sec. III B 3 below, after studying the final-state momentum distribution. Elimination of the final-state interaction with the substrate (by setting $V_C \equiv 0$), reduces the model wave function $\psi_{k_{f,z}}(z)$ in (6) to the final-state wave function applied in Refs. [8,48].

2. Momentum-space analysis

To further characterize the conditions for the occurrence of a substrate resonance in the final photoelectron state $\Psi^f_{\mathbf{k}_f}$ (6), we examine its Cartesian component along the surface normal in momentum representation, $\tilde{\psi}_{k_{f,z}}(k)$. In Appendix A we show that the momentum distribution $\tilde{\psi}^{\rm WBK,0}_{k_{f,z}}(k)$ of a zero-order WKB-type analytical approximation [not to be confused with the numerical first-order WKB solution $\psi^{\rm WBK,1}_{k_{f,z}}(z)$ in Fig. 3(c)] for the wave function of an electron in an infinitely extended bulk potential $V^{\rm bulk}_C(z') = A_{10} + A_1 \cos[2\pi z'/a_s]$, that oscillates along the entire z axis in the same way as the Chulkov potential V_C (11) alternates inside the bulk, has dominant momentum contributions at the momenta $k^{(j,\pm)}_C = \pm k_C + j k_{\rm latt}$, where

$$k_C = \sqrt{2(\varepsilon_{f,z} - A_{10}/A_0)}. \tag{13}$$

These momenta are replicas of $\pm k_C$, shifted into different Brillouin zones by integer multiples j of the reciprocal momentum $k_{\rm latt} = 2\pi/a_s = 1.595$ a.u.. This characteristic transcends to the momentum-space probability distribution along the surface normal of the exact photoelectron final state. Its square root, $|\tilde{\psi}_{k_{f,z}}(k)|$, is shown off resonance ($\varepsilon_{f,z} = 13.65$ eV) in Figs. 5(a) and 5(b) and at resonance ($\varepsilon^{\rm res}_{f,z} = 23.94$ eV) in Fig. 5(c). The distributions in Fig. 5 are the Fourier transforms of the wave functions calculated numerically by propagating $\psi_{k_{f,z}}(z)$ backwards (toward decreasing values of z), starting at $z = 60$ a.u. and imposing *outgoing*-wave boundary conditions

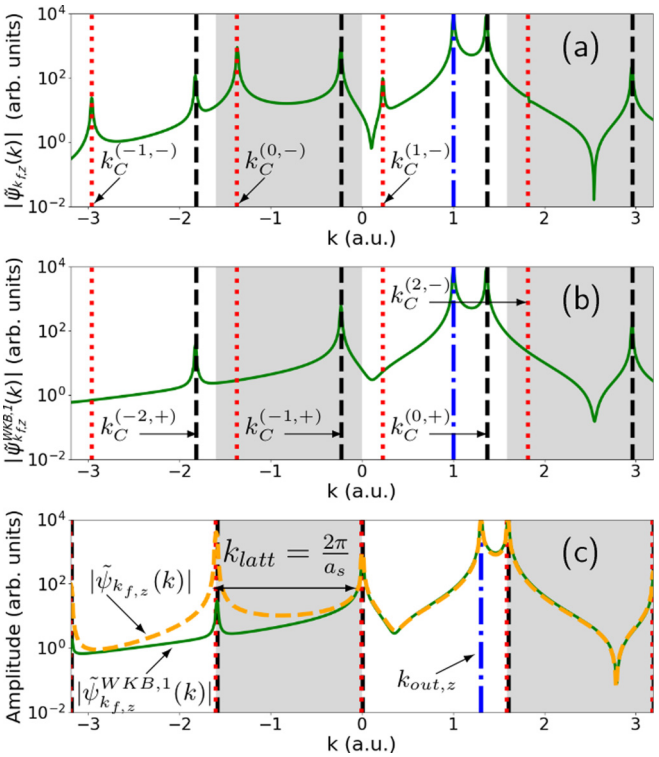

FIG. 5. Momentum-space final-state wavefunction amplitudes $|\tilde{\psi}_{k_{f,z}}(k)|$ in Eq. (6) along the surface normal. (a) Off resonance for $\varepsilon_{f,z} = 13.65$ eV. (b) Off resonance for the approximate wavefunction $|\tilde{\psi}^{\mathrm{WKB},1}_{k_{f,z}}(k)|$ for $\varepsilon_{f,z} = 13.65$ eV. (c) $|\tilde{\psi}_{k_{f,z}}(k)|$ (dashed orange line) and $|\tilde{\psi}^{\mathrm{WKB},1}_{k_{f,z}}(k)|$ (solid green line) at the resonance energy $\varepsilon^{\mathrm{res}}_{f,z} = 23.94$ eV. Adjacent Brillouin zones are distinguished by the alternating shaded and unshaded background. Dash-dotted blue vertical lines mark the asymptotic momentum $k_{\mathrm{out,z}} = \sqrt{2\varepsilon_{f,z}}$. Dashed black lines and dotted red lines indicate the momenta $k_C^{(j,+)} = k_C + jk_{\mathrm{latt}}$ and $k_C^{(j,-)} = -k_C + jk_{\mathrm{latt}}$, respectively, that are derived analytically from $\tilde{\psi}^{\mathrm{WKB},1}_{k_{f,z}}(k)$ in Appendix A.

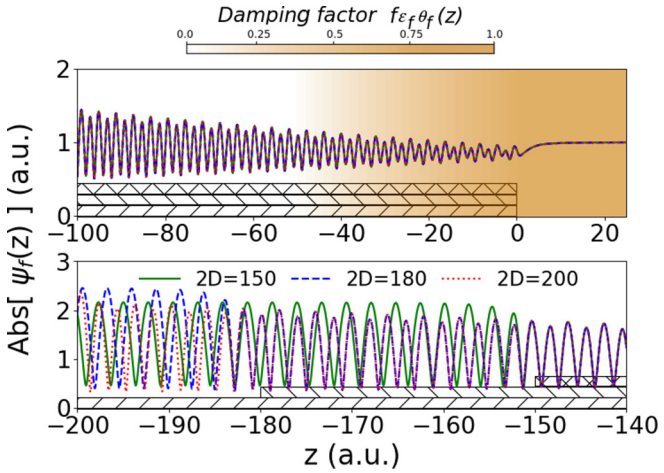

FIG. 6. Amplitude of the final-state-wave-function component along the surface normal, $\psi_{k_{f,z}}(z)$, at resonance for Cu(111) slab thicknesses $2D = 150$, 180, and 200 a.u., within the top 100 a.u. from the exit surface at $z = 0$. For $z \in [-200, -140]$. The intensity of the orange/gray background color illustrates the decreasing photoelectron escape probability due to the finite photoelectron mean-free path. The slabs are indicated by the hatched bars at the bottom of each panel.

$\psi_{k_{f,z}}(z) \to \exp[ik_{\mathrm{out,z}}z]$ with asymptotic momentum $k_{\mathrm{out,z}} = \sqrt{2\varepsilon_{f,z}}$. These calculations were performed for the parameter values $A_1 = 5.14$ eV and $A_{10} = -11.895$ eV of Ref. [29]. In addition to the concentration of the bulk-wave-function momentum distribution $|\tilde{\psi}^{\mathrm{WBK},0}_{k_{f,z}}(k)|$ at each $k_C^{(j,\pm)}$ (see Appendix A), $|\tilde{\psi}^{\mathrm{WBK},1}_{k_{f,z}}(k)|$ and $|\tilde{\psi}_{k_{f,z}}(k)|$ peak, as expected, at the asymptotic momentum $k_{\mathrm{out,z}} = \sqrt{2\varepsilon_{f,z}}$ of the ejected photoelectron.

The outgoing-wave boundary condition imposed on the exact solution in Fig. 5(a) results in comparatively small probability densities at the incoming momenta $k_C^{(j,-)}$ with respect to the outgoing momenta $k_C^{(j',+)}$. This is even more prominent for the momentum distribution of the first-order WKB wave function $\psi^{\mathrm{WBK},1}_{k_{f,z}}(z)$ calculated under the same condition as the distribution in Fig. 5(a). The distributions $|\tilde{\psi}_{k_{f,z}}(k)|$ and $|\tilde{\psi}^{\mathrm{WBK},1}_{k_{f,z}}(k)|$ in Figs. 5(a) and 5(b) present similar profiles for positive momenta, but differ at negative k. Because of the enforced outgoing-wave boundary condition and the construction of $\psi^{\mathrm{WBK},1}_{k_{f,z}}(z)$ (see Appendix A), no significant contributions at $k_C^{(j,-)}$ are present in $\tilde{\psi}^{\mathrm{WBK},1}_{k_{f,z}}(k)$. This means that our WKB model excludes wave-function reflections, which in turn prevents the final-state resonance from being built up and leads to nonresonant RABBITT spectra and phases.

We observe the resonance phenomenon discussed in the previous section to occur when the condition $k_C \approx k_{\mathrm{latt}}$ is met, i.e., when the final-state bulk-momentum distribution peaks very close to or at the reciprocal momenta $j\,k_{\mathrm{latt}}$. Figure 5(c) shows both $|\tilde{\psi}^{\mathrm{WBK},1}_{k_{f,z}}(k)|$ and $|\tilde{\psi}_{k_{f,z}}(k)|$. The exact solution possesses a significantly more prominent peak at $k = -k_{\mathrm{latt}}$ than the WKB-model wave function. This is due to the suppression of wave-function reflections throughout the substrate in $\psi^{\mathrm{WKB},1}_{k_{f,z}}$. It supports the resonant phenomenon observed in the RABBITT phases in Ref. [20] being due to the final-state interaction with the corrugated substrate.

The absence of peaks at momenta $k_C^{(j,-)}$ in the first-order WKB amplitude $|\tilde{\psi}^{\mathrm{WBK},1}_{k_{f,z}}(k)|$ in Fig. 5(b) is consistent with the lack of reflected wave-function contributions. In contrast, the occurrence of peaks at momenta $k_C^{(j,-)}$ and $k_C^{(j,+)}$ in the numerical solution shown in $|\tilde{\psi}_{k_{f,z}}(k)|$ in Fig. 5(a) demonstrates that the resonant amplitude increase in the full solution is due the superposition of wave-function components that propagate in opposite directions with comparable amplitudes. This results in a final-state momentum distribution that largely resembles a stationary state. This stationary-state character, rather than a purely outgoing-wave behavior, of the full numerical solution is also expressed as oscillations of the absolute value of the wave-function amplitude inside the substrate in Fig. 6. The numerical observation that at resonance $k_C \approx k_{\mathrm{latt}}$ further demonstrates that the periodic oscillations of the bulk potential can strongly influence photoelectrons that are released by XUV-photon absorption into superpositions of continuum states of the substrate. The resonance condition $k_C \approx k_{\mathrm{latt}}$ and Eq. (13) allow the adjustment of the

potential-depth parameter A_{10} in Eq. (11) to the resonance energy $\varepsilon_f^{\rm res} \approx 24$ eV that can be estimated from the experimental RABBITT phases in Ref. [20]. For the photoelectron-emission direction $\theta_f = 30^\circ$ and $\varepsilon_{f,z} \approx 18$ eV, we obtain $A_{10} \approx (\varepsilon_{f,z} - 0.5k_{\rm latt}^2)A_0 = -16.58$ eV. The relaxation of A_{10} from its original value in Ref. [29] is justified in the following Sec. III B 3.

At resonance, back-and-forth wave-function reflections in the bulk potential lead to an amplitude enhancement of the photoelectron wave function inside the solid that becomes observable in photoemission spectra. This enhancement is a purely quantum-mechanical effect and occurs only when the de Broglie wavelength of the photoelectron matches the substrate's interlayer distance, in agreement with the numerical results shown in Figs. 3(a)–3(c) and 5.

We note that the present analysis only addresses the crystal periodicity along the surface normal, while in a full three-dimensional model the final-state wave function is characterized by additional momentum components. These added momentum components emerge due to the A-B-C stacking of layers in Cu(111) and depend on the crystal orientation and emission direction. However, with regard to the A-B-C stacking, a characteristic length of $3a_s$ entails 9 times lower energies that are outside the range of photoelectron energies of relevance in the present study.

3. Closer examination of the dependence on the substrate-potential-oscillation amplitude

As noted in Sec. III B 1 above, the corrugation parameter A_1 in the model-substrate potential V_C given by Eq. (11) affects the photoelectron final state. For increasing values of A_1 the final-state wave function $\psi_{k_{f,z}}(z)$ becomes increasingly localized near the atomic cores of the substrate. At resonance a larger potential-oscillation amplitude was seen in Fig. 3 to promote the increase of the final-state amplitude inside the solid significantly. Even though the resonance energy $\varepsilon_{f,z}^{\rm res}$ can be assumed to be independent of A_1 within the range of parameter values $A_1 = 5.14$ and 7.71 eV this assumption breaks down if a larger parameter range is considered.

To quantify the interdependence of $\varepsilon_{f,z}^{\rm res}$ and A_1, we show in Fig. 7 the maximum of the wave-function amplitude, $\max(|\psi_{k_{f,z}}(z)|)$, within the top 100 a.u. from the emission surface (for $z \in [-100, 0]$ a.u.) as a function of the photoelectron kinetic energy $\varepsilon_{f,z}$ and of A_1 for the potential-depth parameter value $A_{10} = -16.58$ eV. For this value of A_{10} the resonance energy $\varepsilon_f^{\rm res}$ and its component along the z axis $\varepsilon_{f,z}^{\rm res}$ match the experimental values of approximately 24 and 18 eV in Ref. [20]. We note that the resonance energy $\varepsilon_{f,z}^{\rm res}$ is seen to depend weakly on A_1, the main effect being that the resonant wave-function amplitude inside the substrate significantly increases as A_1 grows. The resonance energy, indicated by the dash-dotted thick white line, shows a moderate upward shift of $\varepsilon_{f,z}^{\rm res}$ as A_1 increases from 7 eV to ≈15 eV. The orange dashed lines indicates energies $\varepsilon_{f,z}$ on either side of the central resonance energy $\varepsilon_{f,z}^{\rm res}$ where $\max(|\psi_{k_{f,z}}(z)|)$ dropped to one half of its values at resonance. The light-blue solid line shows the variation of $\varepsilon_{f,z}^{\rm res}$ with A_1 deduced from the momentum matching condition $k_C = k_{\rm latt}$ for $|\psi_{k_{f,z}}^{\rm WKB,0}(z)|$ in Appendices A and B. Even though the WKB solution does not contain the resonant amplitude growth of the exact solution [cf. Fig. 3(c)], the variation of $\varepsilon_{f,z}^{\rm res}$ with A_1 agrees well with the numerically determined resonance energy from the exact $\psi_{k_{f,z}}(z)$.

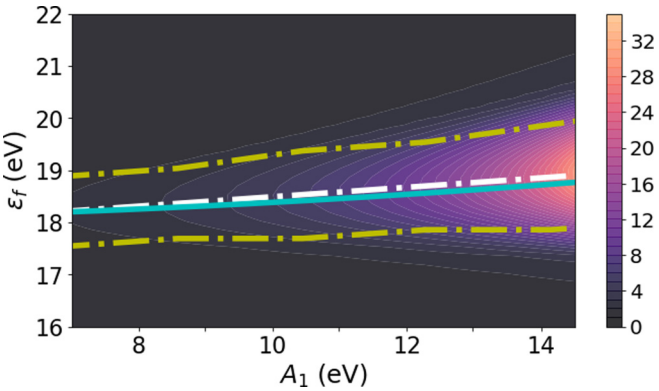

FIG. 7. Maximum of the final-state wave-function amplitude $\max(|\psi_{k_{f,z}}(z)|)$ within the top 100 a.u. from the emission surface as a function of the photoelectron kinetic energy $\varepsilon_{f,z}$ and the Cu(111) bulk-potential-oscillation amplitude A_1. The dash-dotted white line indicates the resonant energy $\varepsilon_{f,z}^{\rm res}$ and yellow dashed lines the half widths of $\max(|\psi_{k_{f,z}}(z)|)$. The solid light blue line shows the resonance energy deduced analytically from the momentum-matching condition $k_C = k_{\rm latt}$.

By employing the parameters published in Ref. [29] for the potential depth $A_{10} = -11.895$ eV and oscillation amplitude $A_1 = 5.14$ eV in the parametrization (11) of the substrate potential V_C, we cannot reproduce the resonance energy $\varepsilon_f^{\rm res} \approx 24$ eV, deduced from the photoemission spectra in Ref. [20]. This discrepancy might be expected, since the potential parameters in Ref. [29] are specifically adjusted to provide surface-state, band-gap, and image-states energies in agreement with time-independent photoemission measurements and previous calculations (see [29] and references therein). In contrast to our fitting procedure, the parameters given in Ref. [29] are not optimized to yield adequate photoelectron continuum states, capable of reproducing details of interferometric photoemission spectra. We thus do not consider the particular parameter values for V_C in Ref. [29] to be suitable for the present study, and we allow for a readjustment of the parameters A_{10} and A_1 in Secs. III C and III D below.

4. Slab-thickness independence

To ensure that the slab used in our numerical calculation is sufficiently thick to prevent the resonant final-state-amplitude increase inside the substrate to depend on the slab widths $2D$, we examined the dependence of the final-state wave-function component along the surface normal, $\psi_{k_{f,z}}(z)$, and interferometric photoemission spectra on D.

Figure 6 shows the amplitude of $\psi_{k_{f,z}}(z)$ calculated at the resonant energy $\varepsilon_f^{\rm res} = 24$ eV (i.e. $\varepsilon_{f,z}^{\rm res} = 18$ eV) for three values of D. The numerical results in this figure were obtained for the parameter $A_1 = 5.14$ eV of Ref. [29] and for the value $A_{10} = -16.58$ eV that matches the calculated to the measured resonance energy. Note the value for A_1 will be readjusted below. As Fig. 6(a) demonstrates, the amplitude increase is equally reproduced for $2D = 150$, 180, and 200 a.u. inside the slabs. Interferometric spectra based on Eq. (12)

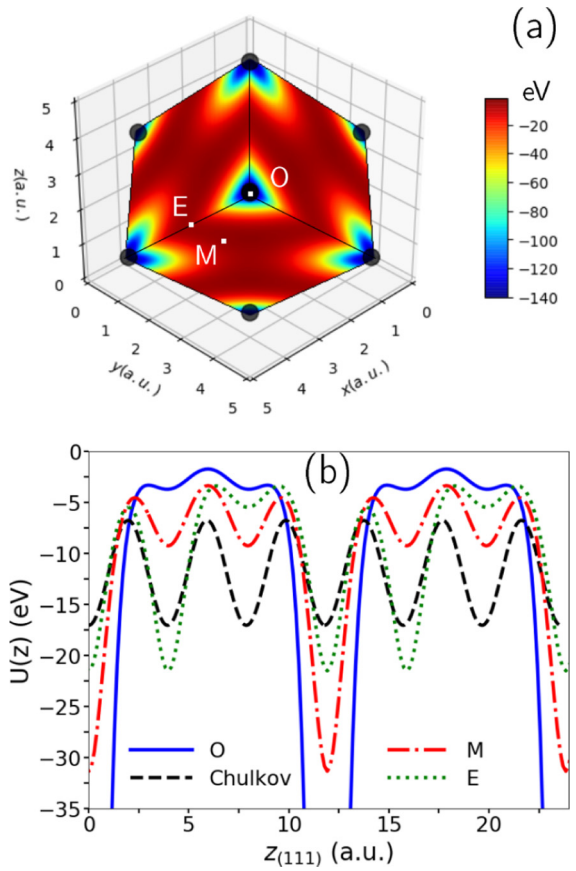

FIG. 8. (a) DFT-calculated effective potential for Cu displayed over a single unit cell, obtained using the GPAW package [49,50]. Lattice points are indicated by black dots. The [111] crystallographic direction is oriented perpendicular to the page. (b) Lineouts of the three-dimensional DFT potential in (a) along the [111] direction, traversing two unit cells at the points O, M, and E indicated as small white squares in (a). Also shown is the parametrization of the substrate potential V_C according to Ref. [29] (dashed black line). The potential zero for the DFT calculation is adjusted by setting the Fermi energy equal to the experimental value for Cu(111) of 4.94 eV [31].

are not sensitive to inaccuracies in the final-state modeling at distances larger than a few photoelectron-escape depths. A slab thickness of 150 a.u is therefore sufficient for modeling the final-state wave function.

5. Comparison of the substrate potential $V_C(z)$ with a three-dimensional DFT potential

To provide an illustration for the three-dimensional electronic structure, we applied the GPAW software package [49,50] to calculate the three-dimensional potential shown in Fig. 8(a). In this DFT calculation we used $24 \times 24 \times 24$ spatial grid points per unit cell of the face-centered cubic periodic lattice of Cu and a Perdew-Burke-Ernzerhof exchange-correlation functional [51]. Figure 8(b) compares the Cu(111) model potential V_C based on the parameters determined by Chulkov [29] (dashed black line) with lineouts along the [111] direction of the DFT potential in Fig. 8(a), where the [111] direction is oriented perpendicular to the page. The lineouts are taken at the points O, M, and E in the Cu(111) unit cell indicated, as white dots in Fig. 8(a).

The lineouts at different points in the Cu(111) unit cell and the planar potential average strongly deviate from each other and from the Chulkov parametrization in Ref. [29] [Fig. 8(b)]. In particular, the simple sinusoidal oscillation inside the substrate with period a_s of the Chulkov model potential (11) is replaced by a superposition of spatial oscillations with more than one wavelength. The photoelectron is therefore exposed to an effective interaction with the substrate with a spatial variation that might not be adequately represented by a single length a_s. An example of an analytical potential with more than one wavelength component is found in the one-dimensional time-dependent Schrödinger equation study of Borisov *et al.* [52], where a combination of a Chulkov potential V_C and a periodic assembly of Gaussian potentials is applied to describe time-resolved (streaked) photoemission from a Mg(0001) surface.

In the interest of elucidating the basic physical process behind the expression of substrate-dependent final-state resonance effects in RABBITT spectra and phases, we do not attempt to represent the spatial variation of the photoelectron-substrate interaction in terms of a more elaborate (multiwavelength) effective potential. Instead, we adhere to the functional form of V_C given in Eq. (11), but allow for deviations from the potential parameters A_1 and A_{10} for Cu(111) in Ref. [29].

C. RABBITT spectra

Figures 9(a) and 9(b) show interferometric photoemission spectra calculated according to Eqs. (1) and (12), based on either the approximate first-order WKB final-state wavefunction component $\psi^{\mathrm{WKB},1}_{k_{f,z}}(z)$ or on the exact numerical final-state wave function component $\psi_{k_{f,z}}(z)$, respectively. Both spectra are derived for the corrugation parameter $A_1 = 13.52$ eV, potential-depth parameter $A_{10} = -16.58$ eV, and the photoemission angle $\theta_f = 30^\circ$ of Ref. [20].

The spectra are characterized by delay-dependent HH emission and SB yields. The spectral yields in Fig. 9 are normalized to the maximal yield in Fig. 9(b). The SB-yield oscillations display energy-dependent phase shifts that are more pronounced in the calculations with the exact numerical solution $\psi_{k_{f,z}}(z)$ in Fig. 9(b) than for the approximated WKB final states in Fig. 9(a). The photoemission yields for the exact final state in Fig. 9(b) tend to be higher than the yields we obtain for WKB-approximated final states in Fig. 9(a) and have stronger energy-dependent SB- and HH-yield enhancements for photoelectron kinetic energies between approximately 22 and 25 eV. The final-state resonance at SB20 creates a very visible yield increase that extends over several eV. It qualitatively agrees with the observations made in Ref. [10] for measured RABBITT spectra from Ni(111) surfaces.

D. RABBITT phases

We determine the RABBITT phases in our calculated spectra by integrating the photoemission yield $P(\varepsilon_f, \tau)$ over ε_f. We choose 0.5 eV-wide integration intervals centered at the central SB energies. This results in energy-integrated SB yields $P^{(2n)}(\tau)$, which, for any given SB order $2n$, we fit to the

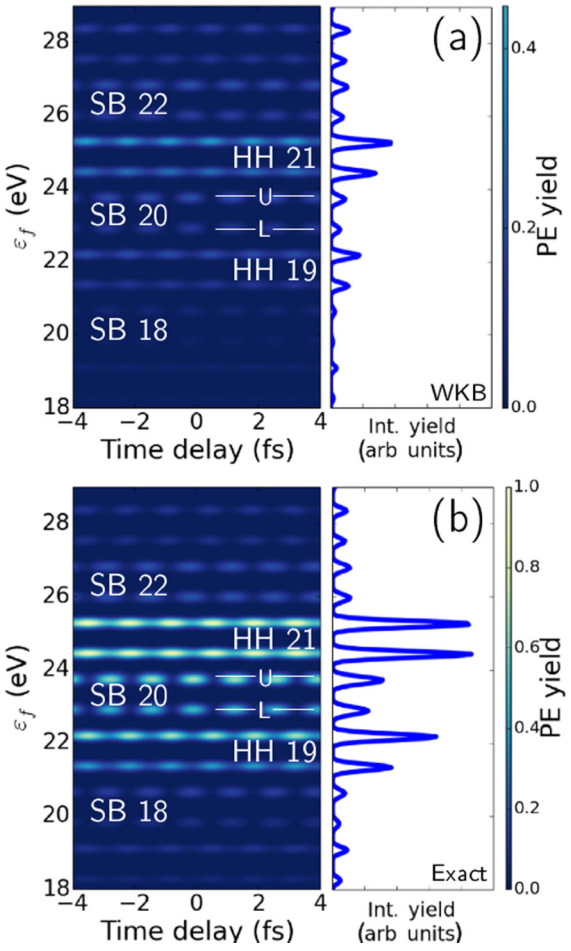

FIG. 9. Calculated RABBITT spectrum as a function of the photoelectron kinetic energy ε_f for emission from the lower (L) and upper (U) $3d$-valence bands of Cu(111), based on the (a) approximate first-order WKB final-state wave function $\psi_{k_{f,z}}^{\mathrm{WKB},1}(z)$ and (b) exact numerical final-state wave function $\psi_{k_{f,z}}(z)$. The spectra in (a) and (b) are normalized to the highest yield in (b). Panels to the right of the color-coded spectra show the corresponding τ-integrated yields. Labels "SB 2n" and "HH 2n + 1" indicate sideband and harmonic emission orders.

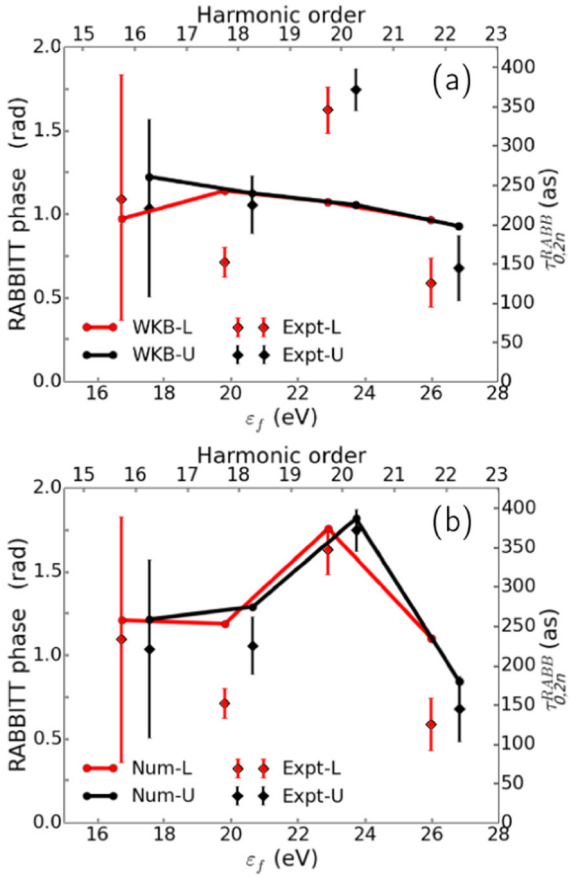

FIG. 10. RABBITT phases $\phi_{0,2n}^{\mathrm{RAB}}$ and corresponding spectral photoemission-time delays $\tau_{0,2n}^{\mathrm{RAB}}$, excluding the Fresnel-reflection contribution $2\phi^{\mathrm{Fres}}$, as a function of the photoelectron kinetic energy ε_f. (a) Phases for emission from the lower and upper $3d$-valence bands of Cu(111), denoted as "WKB-L" and "WKB-U," respectively, deduced from the spectrum in Fig. 9(a) [i.e., calculated based on the approximate first-order WKB final-state wave function $\psi_{k_{f,z}}^{\mathrm{WKB},1}(z)$]. (b) As (a) but deduced from the spectrum in Fig. 9(b) [i.e., calculated based on the exact numerical final-state wave function $\psi_{k_{f,z}}(z)$]. The corresponding phases derived in Ref. [20] from measured RABBITT spectra are labeled as "Expt-L" and "Expt-U." Solid red and black lines are added only to guide the eye.

expression

$$P^{(2n)}(\tau) = \left[a_1 \cos\left(2\omega_{\mathrm{IR}}\tau - \phi_{2n}^{\mathrm{RAB}}\right) + a_2\right] \times \exp\left[-\frac{(\tau - a_3)}{a_4}\right]^2 + a_5 \tag{14}$$

by adjusting ϕ_{2n}^{RAB} and the parameters $a_1, \ldots, a_5$.

1. Comparison with measured spectral phases and photoemission-time delays

The energy-dependent RABBITT phases

$$\phi_{2n}^{\mathrm{RAB}} = 2\phi^{\mathrm{Fres}} + \phi_{0,2n}^{\mathrm{RAB}} \tag{15}$$

contain the contribution $\phi^{\mathrm{Fres}} = \arg\left[\mathbf{k}_f \cdot \mathbf{E}_{\mathrm{IR}}^{\mathrm{out}}(t_d = 0)\right]$. It arises from the Fresnel reflection of the assisting IR pulse at the surface, which is included in our model [19,22,24,53]. The experimental RABBITT phases in Ref. [20] are given after subtraction of the theoretically calculated values of $2\phi^{\mathrm{Fres}}$. Accordingly, we show in Fig. 10 RABBITT phases $\phi_{0,2n}^{\mathrm{RAB}}$ after subtracting our calculated Fresnel term ($2\phi^{\mathrm{Fres}} = 1.524$ rad), in order to facilitate a direct comparison with the experimental data. The right vertical axis translates the Fresnel-corrected phases $\phi_{0,2n}^{\mathrm{RAB}}$ to the spectral photoemission-time delays $\tau_{0,2n}^{\mathrm{RAB}} = \phi_{0,2n}^{\mathrm{RAB}}/(2\omega_{\mathrm{IR}})$.

The RABBITT phases $\phi_{0,2n}^{\mathrm{RAB}}$ and corresponding spectral photoemission-time delays $\tau_{0,2n}^{\mathrm{RAB}}$ in Fig. 10(a) are derived from the spectrum in Fig. 9(a) and thus based on the approximate first-order WKB final-state wave function $\psi_{k_{f,z}}^{\mathrm{WKB},1}(z)$. They resolve photoemission from the lower and upper $3d$-valence bands of Cu(111) and tend to follow the experimental data for the HH orders $2n = 16$, 18, and 22. However, they clearly fail in matching the experimentally observed large phase increase of $\phi_{0,20}^{\mathrm{RAB}}$ at HH order $2n = 20$. This lack in

reproducing the experimental phase increase near the resonance energy is due to the absence of the amplitude enhancement inside the substrate of the approximate final-state wave function $\psi_{k_{f,z}}^{\mathrm{WKB},1}(z)$ [see Figs. 3(a)–3(b)], as we will further examine next.

In contrast, the RABBITT phases and corresponding spectral photoemission-time delays in Fig. 10(b), calculated based on the exact numerical final-state wave function $\psi_{k_{f,z}}(z)$, are in better agreement with the experimental prediction and, in particular, match the measured resonant enhancement near SB order $2n = 20$. This provides strong evidence for the resonant local phase increase at SB20 being due to the resonant interaction between the excited photoelectron and the substrate. In view of the shift in final-state wave function probability density away from the exit surface towards the bulk seen in Fig. 3(b), the resonantly increased photoemission-time delay can thus be interpreted as an increased propagation time of the excited photoelectron in the solid that is due to an augmented photoemission from deeper inside the substrate. Off resonance, the final-state amplitude enhancement inside the solid vanishes, consistent with (i) the agreement between calculated phases and time delays in Figs. 10(a) and 10(b) and (ii) a necessary condition for the measured resonance effect being that the photoelectron de Broglie wavelength matches the periodicity of the substrate potential.

With regard to both the resonant increase of RABBITT phases measured in Ref. [20] and no significant energy dependence of Cu(111) RABBITT phases observed experimentally for a slightly different IR frequency, $\omega_{\mathrm{IR}} = 1.577$ eV, at two pulse-incidence and electron-emission geometries in Ref. [19], we conclude that the resonant phase increase in interferometric photoemission from solids depends on

(i) the material, lattice type, and crystal orientation of the substrate,

(ii) the IR-photon energy used to drive the HH-generation process and related XUV-photon energies allowing photoemission near resonance, and

(iii) the IR-pulse and XUV-APT incidence angle and the photoelectron detection solid angle, which determine the photoelectron kinetic energy $\varepsilon_{f,z}$.

2. *Dependence on the bulk-potential-oscillation amplitude*

Figure 11 shows the dependence of our calculated RABBITT phases $\phi_{0,2n}^{\mathrm{RAB}}$ and corresponding spectral photoemission-time delays $\tau_{0,2n}^{\mathrm{RAB}}$ on the corrugation amplitude $A_1 \in [7.52, 15.52]$ eV of the model substrate potential V_C given by Eq. (11). Numerical results for photoemission from the lower and upper $3d$-valence bands of Cu(111) are displayed separately in Figs. 11(a) and 11(b). With the exception of A_1, all other substrate, IR-pulse, and XUV-APT parameters are identical with the parameters used for the simulations in Fig. 10(b). The numerical results in Fig. 11 demonstrate an increasingly strong augmentation of the phases and time delays for increasing A_1 near the resonance energy, while off resonance the influence of A_1 is comparatively very small. As discussed in Secs. III B 1 and III B 3 above, the final-state resonance becoming more pronounced as A_1 increases is due to the resonant increase of the final-state probability density getting more significant for larger values of A_1. This

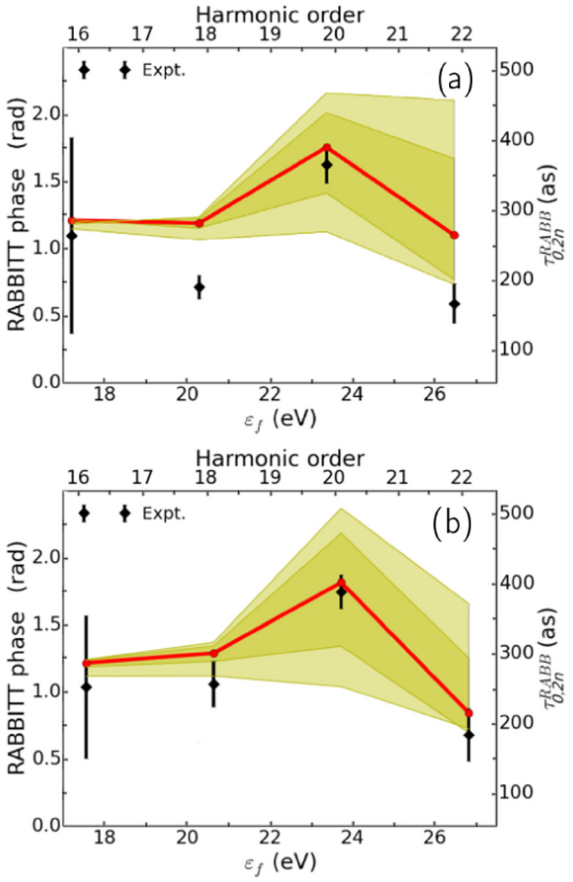

FIG. 11. RABBITT phases $\phi_{0,2n}^{\mathrm{RAB}}$ and corresponding spectral photoemission-time delays $\tau_{0,2n}^{\mathrm{RAB}}$, excluding the Fresnel-reflection contribution $2\phi^{\mathrm{Fres}}$, as a function of the photoelectron kinetic energy ε_f. Results calculated with the exact numerical final-state wave function $\psi_{k_{f,z}}(z)$. Dependence on the oscillation amplitude A_1 of the model-substrate potential V_C for emission from the (a) lower and (b) upper $3d$-valence bands of Cu(111). Solid red dots and lines show the best overall agreement with the experimental data in Ref. [20] obtained for $A_1 = 13.52$ eV. The lines are added only to guide the eye. Variations of the RABBITT-phase and photoemission delays for $A_1 \in [10.52, 15.52]$ eV and $A_1 \in [7.52, 16.57]$ eV are shown as the darker and lighter green shaded area, respectively. The lower and upper A_1 values for each interval correspond to the respective lower and upper phase-interval limits. With the exception of A_1, all other substrate, IR-pulse, and XUV-APT parameters are identical with the parameters used in the simulations in Fig. 10(b).

is consistent with a (on average) larger photoelectron transport time [cf. Figs. 3(b), 3(d), and 7].

On resonance, $A_1 \in [10.52, 15.52]$ eV and the assumed transport velocity $k_{\mathrm{latt}} = 1.59$ a.u. lead to photoelectron-transport times in the substrate between 320 and 420 as (corresponding to effective escape depths between 21.0 and 27.6 a.u.) for emission from the L band [Fig. 11(a)] and to transport times between 300 and 450 as (corresponding to effective escape depths between 19.7 and 29.6 a.u.) for emission from the U band [Fig. 11(b)]. The variation of A_1 within $[7.52, 16.57]$ eV widens the transport-time intervals to $[260, 450]$ as (corresponding to effective escape depths between 17.1 and 29.6 a.u.) and to $[240, 500]$ as

(corresponding to effective escape depths between 15.8 and 32.9 a.u.), respectively for L- and U-band emission.

As indicated in Fig. 8, the potential oscillation along different electron trajectories in the solid can differ significantly from the sinusoidal variation assumed in the one-dimensional model potential V_C of Ref. [29]. However, if a final-state resonance can be identified in experimental RABBITT phases, the effective oscillation amplitude felt by the photoelectron in the solid can be estimated within our model. This estimate consists in first performing a simulation for a uniform bulk potential by setting $A_1 = 0$ in order to establish a baseline for nonresonant emission. Next, A_1 is adjusted to the best overall fit of all available experimental RABBITT phases, including resonant and nonresonant energies. Applied to different emission geometries and surface orientations, this scheme will return different values for A_1. We speculate that probing sufficiently many emission directions might allow the reconstruction of the effective substrate potential in full dimensionality.

IV. SUMMARY AND OUTLOOK

We calculated interferometric electron spectra and phases for photoemission from the $3d$-valence band of Cu(111) surfaces. Our numerical results are based on a quantum-mechanical model developed with particular emphasis on the interaction of the excited photoelectron with the substrate. We numerically evaluated the transition amplitude in the nondipole velocity gauge between translationally invariant initial valence-band states and final states that include the influence of the periodic substrate potential and the inhomogeneous electric field of the Fresnel-reflected IR pulse on the photoelectron. Our numerical results demonstrate the sensitive response of interferometric photoelectron spectra to photoelectron propagation in the substrate and reproduce the measured resonantly enhanced increase of RABBITT phases and associated spectral photoemission-time delays published in Ref. [20].

Within our model, the experimentally observed final-state resonance is traced to the resonant enhancement of the final-state wave-function amplitude in the substrate and can be interpreted as an increased photoelectron-propagation time. The increased propagation time is commensurate with an effective shift of the final-state probability density away from the exit surface into the bulk, i.e., with an effective increase of the photoelectron-escape depth at resonance. Based on the identification of final-state resonances in measured RABBITT-phase differences, we suggest a method for determining the effective bulk-potential-oscillation amplitude felt by the photoelectron in the solid.

ACKNOWLEDGMENTS

We thank L. Gallmann, U. Keller, and M. Murnane for stimuating discussions. This work was supported by the Chemical Sciences, Geosciences, and Biosciences Division, Office of Basic Energy Sciences, Office of Science, US Department of Energy under Award No. DEFG02-86ER13491 (attosecond interferometry, photoelectron final states in spatially varying external fields) and the U.S. National Science Foundation (NSF) under Award No. PHY 1802085 (general theory and numerical tools development for photoemission from surfaces).

APPENDIX A: WKB EXPANSION AND MOMENTUM COMPOSITION OF COSINE-POTENTIAL POSITIVE-ENERGY STATES

The Wentzel-Kramers-Brillouin (WKB) approximation provides semiclassical solutions

$$\psi^{\mathrm{WKB}}_{k_{f,z}}(z) = e^{i\hbar S(z)} \tag{A1}$$

of the Schrödinger equation with $S(z) = S_0(z) - i\hbar S_1(z) + O(\hbar^2)$ [47]. For the following analysis we first examine the zeroth order WKB function $\psi^{\mathrm{WKB},0}_f(z) = e^{i\hbar S_0(z)}$ for the infinitely extended potential $V_C^{\mathrm{bulk}} = A_{10} + A_1 \cos(\frac{2\pi}{a_s} z')$ that equals the bulk part of the Chulkov potential in Eq. (11),

$$\psi^{\mathrm{WKB},0}_{k_{f,z}}(z) \sim e^{\pm i \int_{z_0}^{z} k(z')dz'}, \tag{A2}$$

where

$$k(z) = \sqrt{2[\varepsilon_{f,z} - A_{10}/A_0 + A_1/A_0 \cos k_{\mathrm{latt}} z]} \tag{A3}$$

and $k_{f,z} = \sqrt{2\varepsilon_{f,z}}$. We assume small oscillation amplitudes A_1 and expand

$$\sqrt{1+\eta} = 1 + \tfrac{1}{2}\eta - \tfrac{1}{8}\eta^2 + \tfrac{1}{16}\eta^3 + O(\eta^4), \tag{A4}$$

with $\eta = \eta_0 \cos k_{\mathrm{latt}} z$ and $\eta_0 = \frac{A_1/A_0}{\varepsilon_{f,z} - A_{10}/A_0}$. For all numerical applications in this work $|\eta| \lessapprox 1/3$. For sufficiently fast electrons the local momentum can be approximated as

$$k(z) = k_C\big(1 + \tfrac{1}{2}\eta\big) + O(\eta^2), \tag{A5}$$

with the dominant momentum component k_C,

$$k_C \equiv \sqrt{2(\varepsilon_{f,z} - A_{10}/A_0)}. \tag{A6}$$

To identify secondary momentum components, we expand the exponent in (A2) to order $O(\eta^2)$:

$$\int_{z_0}^{z} k(z')dz' = k_C(z - z_0) + \frac{1}{2} k_C \eta_0 (\sin k_{\mathrm{latt}} z - \sin k_{\mathrm{latt}} z_0) + O(\eta^2). \tag{A7}$$

Using $\sin u = \cos(u - \pi/2)$ and the Jacobi-Anger expansion in Bessel functions J_j,

$$e^{iu\cos\theta} = \sum_{j=-\infty}^{\infty} i^j J_j(u) e^{ij\theta}, \tag{A8}$$

we find

$$\psi^{\mathrm{WKB},0}_{k_{f,z}}(z) \sim e^{\pm i k_C (z - z_0) \pm i \frac{1}{2} k_C \eta_0 \sin k_{\mathrm{latt}} z} \sim e^{\pm i k_C (z - z_0)} \sum_{j=-\infty}^{\infty} J_j\left(\frac{1}{2} k_C \eta_0\right) e^{ijk_{\mathrm{latt}} z}, \tag{A9}$$

where we recognize the principal-momentum component k_C with replicas shifted by multiples of the reciprocal momentum k_{latt} into different Brillouin zones as seen in Fig. 5.

For the momentum-space wave functions in Fig. 5(c) and the photoemission spectra and RABBITT phases in Figs. 9(a)

and 10(a), we approximate the final photoelectron state by numerically calculating the first-order WKB wave function $\psi_f^{\mathrm{WKB},1}(z)$ as a solution for the Chulkov potential (11) for the semi-infinite Cu(111) substrate:

$$\psi_{k_{f,z}}^{\mathrm{WKB},1}(z) = \frac{1}{\sqrt{|k(z)|}} e^{+i\int_{z_0}^{z} k(z')dz'}. \tag{A10}$$

With the "+" sign in the exponent we emphasize that $\psi_{k_{f,z}}^{\mathrm{WKB},1}$ is restricted to *positive* local momenta, thus preventing wavefunction reflections inside the substrate in the direction opposite to the emission direction.

APPENDIX B: A_1 DEPENDENCE OF THE DOMINANT MOMENTUM AND HIGHER ORDER REPLICAS

Even when the oscillation amplitude A_1 is not very small (as assumed in Appendix A), and thus $\sqrt{1+\eta} \approx 1+\eta/2$ is a poor approximation, the final-state momentum-space probability density is still peaked at replicas of k_C that are shifted by integer multiples of k_{latt}. To show this, we include the second-order term of the square-root expansion (A4) in (A3) and note that the squared cosine in η^2 can be rewritten as

$$\cos^2 k_{\mathrm{latt}} z = \tfrac{1}{2}[1+\cos(2k_{\mathrm{latt}} z)]. \tag{B1}$$

Second-order contributions ($\sim\eta^2$) introduce not only an oscillatory term, $\cos(2k_{\mathrm{latt}} z)$, but also shift the dominant momentum component k_C by

$$\Delta k_C = -\tfrac{1}{16} k_C \eta_0^2. \tag{B2}$$

This shift is observable as a weak dependence of the resonance energy $\varepsilon_{f,z}^{\mathrm{res}}$ on A_1, which can be shown by numerically solving $k_C + \Delta k_C = k_{\mathrm{latt}}$ for $\varepsilon_{f,z} \to \varepsilon_{f,z}^{\mathrm{res}}$. This $\varepsilon_{f,z}^{\mathrm{res}}$ dependence on A_1, found here in the context of an analytical and simplified treatment, is in agreement with the fully numerical results in the main text (cf. Fig. 7).

In analogy to Eq. (B1), the cubic (η^3) term in Eq. (A3) is

$$\cos^3 k_{\mathrm{latt}} z = \tfrac{1}{2}\cos(k_{\mathrm{latt}} z) + \tfrac{1}{4}\cos(2k_{\mathrm{latt}} z) + \tfrac{1}{4}\cos(3k_{\mathrm{latt}} z). \tag{B3}$$

It includes a term that oscillates with wave number $3k_{\mathrm{latt}}$. Therefore, we find that, even when A_1 is comparable in magnitude with $|A_{10}|$, the wave function is expected to contain the dominant momentum k_C and replicas in all Brillouin zones. This can be seen after Jacobi-Anger series expansions of all the trigonometric functions obtained in the exponent of Eq. (A2) by using Eqs. (A3) and (A4).

APPENDIX C: HIGH-CORRUGATION, LOW-ENERGY LIMIT

We show that in this regime $\psi_{k_{f,z}}^{\mathrm{WKB},0}(z)$ exhibits replicas of $k_C \approx 0$ in every Brillouin zone, i.e., at $k = \pm m k_{\mathrm{latt}}$. For $\varepsilon_{f,z} \approx 0$ and $A_1 = -A_{10}$, the local momentum (A3) is

$$k(z) = \sqrt{2\frac{A_1}{A_0}[1+\cos k_{\mathrm{latt}} z]} = \sqrt{4\frac{A_1}{A_0}}\,|\cos(k_{\mathrm{latt}} z/2)|. \tag{C1}$$

Expressing the absolute value of the cosine as a Fourier series,

$$|\cos(k_{\mathrm{latt}} z/2)| = 8\sum_{m=0}^{\infty} \frac{1}{\pi k_{\mathrm{latt}}} \frac{(-1)^m}{1-4m^2} \cos(m k_{\mathrm{latt}} z), \tag{C2}$$

and integrating the local momentum (C1),

$$\int_{z_0}^{z} \cos(m k_{\mathrm{latt}} z')dz' = \frac{1}{m k_{\mathrm{latt}}}(\sin m k_{\mathrm{latt}} z - \sin m k_{\mathrm{latt}} z_0), \tag{C3}$$

leads to

$$\psi_{k_{f,z}}^{\mathrm{WKB},0}(z) = \prod_m C_m^{(0)} \sum_{j=-\infty}^{\infty} (-1)^j J_j(K_m) e^{i j m k_{\mathrm{latt}} z}, \tag{C4}$$

with

$$K_m = \sqrt{\frac{A_1}{A_0}} \frac{16}{\pi m k_{\mathrm{latt}}^2} \frac{(-1)^m}{1-4m^2} \tag{C5}$$

and z-independent coefficients $C_m^{(0)}$. This shows that dominant momentum components appear at integer multiples of k_{latt} in the low-energy and high-corrugation regime.

[1] S. Hüfner, *Photoelectron Spectroscopy, Principles and Applications* (Springer, Berlin, 2003).

[2] C.-G. Wahlström, J. Larsson, A. Persson, T. Starczewski, S. Svanberg, P. Salières, P. Balcou, and A. L'Huillier, Phys. Rev. A **48**, 4709 (1993).

[3] K. J. Schafer and K. C. Kulander, Phys. Rev. Lett. **78**, 638 (1997).

[4] P. M. Paul, E. S. Toma, P. Breger, G. Mullot, F. Augé, P. Balcou, H. G. Muller, and P. Agostini, Science **292**, 1689 (2001).

[5] J. Mauritsson, M. B. Gaarde, and K. J. Schafer, Phys. Rev. A **72**, 013401 (2005).

[6] K. Klünder, J. M. Dahlström, M. Gisselbrecht, T. Fordell, M. Swoboda, D. Guénot, P. Johnsson, J. Caillat, J. Mauritsson, A. Maquet *et al.*, Phys. Rev. Lett. **106**, 143002 (2011).

[7] U. Thumm, Q. Liao, E. M. Bothschafter, F. Süßmann, M. F. Kling, and R. Kienberger, in *The Oxford Handbook of Innovation*, edited by D. Andrew (Wiley, New York, 2015), Chap. 13.

[8] M. J. Ambrosio and U. Thumm, Phys. Rev. A **94**, 063424 (2016).

[9] R. Locher, L. Castiglioni, M. Lucchini, M. Greif, L. Gallmann, J. Osterwalder, M. Hengsberger, and U. Keller, Optica **2**, 405 (2015).

[10] Z. Tao, C. Chen, T. Szilvási, M. Keller, M. Mavrikakis, H. Kapteyn, and M. Murnane, Science **353**, 62 (2016).

[11] C. Chen, Z. Tao, A. Carr, P. Matyba, T. Szilvási, S. Emmerich, M. Piecuch, M. Keller, D. Zusin, S. Eich *et al.*, Proc. Natl. Acad. Sci. USA **114**, E5300 (2017).

[12] R. Kienberger, E. Goulielmakis, M. Uiberacker, A. Baltuska, V. Yakovlev, F. Bammer, A. Scrinzi, T. Westerwalbesloh, U. Kleineberg, U. Heinzmann *et al.*, Nature (London) **427**, 817 (2004).

[13] G. Sansone, E. Benedetti, F. Calegari, C. Vozzi, L. Avaldi, R. Flammini, L. Poletto, P. Villoresi, C. Altucci, R. Velotta *et al.*, Science **314**, 443 (2006).
[14] E. Goulielmakis, M. Schultze, M. Hofstetter, V. S. Yakovlev, J. Gagnon, M. Uiberacker, A. L. Aquila, E. M. Gullikson, D. T. Attwood, R. Kienberger *et al.*, Science **320**, 1614 (2008).
[15] A. L. Cavalieri, N. Muller, T. Uphues, V. S. Yakovlev, A. Baltuska, B. Horvath, B. Schmidt, L. Blumel, R. Holzwarth, S. Hendel *et al.*, Nature (London) **449**, 1029 (2007).
[16] S. Neppl, R. Ernstorfer, E. M. Bothschafter, A. L. Cavalieri, D. Menzel, J. V. Barth, F. Krausz, R. Kienberger, and P. Feulner, Phys. Rev. Lett. **109**, 087401 (2012).
[17] Q. Liao and U. Thumm, Phys. Rev. Lett. **112**, 023602 (2014).
[18] S. Neppl, R. Ernstorfer, A. L. Cavalieri, C. Lemell, G. Wachter, E. Magerl, E. M. Bothschafter, M. Jobst, M. Hofstetter, U. Kleineberg *et al.*, Nature (London) **517**, 342 (2015).
[19] M. Lucchini, L. Castiglioni, L. Kasmi, P. Kliuiev, A. Ludwig, M. Greif, J. Osterwalder, M. Hengsberger, L. Gallmann, and U. Keller, Phys. Rev. Lett. **115**, 137401 (2015).
[20] L. Kasmi, M. Lucchini, L. Castiglioni, P. Kliuiev, J. Osterwalder, M. Hengsberger, L. Gallmann, P. Krüger, and U. Keller, Optica **4**, 1492 (2017).
[21] F. Siek, S. Neb, P. Bartz, M. Hensen, C. Strüber, S. Fiechter, M. Torrent-Sucarrat, V. M. Silkin, E. E. Krasovskii, N. M. Kabachnik *et al.*, Science **357**, 1274 (2017).
[22] M. J. Ambrosio and U. Thumm, Phys. Rev. A **96**, 051403(R) (2017).
[23] M. Ossiander, J. Riemensberger, S. Neppl, M. Mittermair, M. Schäffer, A. Duensing, M. S. Wagner, R. Heider, M. Wurzer, M. Gerl *et al.*, Nature (London) **561**, 374 (2018).
[24] M. J. Ambrosio and U. Thumm, Phys. Rev. A **97**, 043431 (2018).
[25] Q. Liao and U. Thumm, Phys. Rev. A **92**, 031401(R) (2015).
[26] J. Li, E. Saydanzad, and U. Thumm, Phys. Rev. Lett. **120**, 223903 (2018).
[27] E. Saydanzad, J. Li, and U. Thumm, Phys. Rev. A **98**, 063422 (2018).
[28] S. Tanuma, C. J. Powell, and D. R. Penn, Surf. Interface Anal. **43**, 689 (2011).
[29] E. Chulkov, V. Silkin, and P. Echenique, Surf. Sci. **437**, 330 (1999).
[30] E. Palik, *Handbook of Optical Constants in Solids* (Academic, San Diego, 1998).
[31] H. L. Skriver and N. M. Rosengaard, Phys. Rev. B **46**, 7157 (1992).
[32] A. L. Frapiccini, G. Gasaneo, F. Colavecchia, and D. Mitnik, J. Electron Spectrosc. **161**, 199 (2007).
[33] M. J. Ambrosio, J. A. Del Punta, K. V. Rodriguez, G. Gasaneo, and L. U. Ancarani, J. Phys. A **45**, 015201 (2012).
[34] M. J. Ambrosio, D. M. Mitnik, L. U. Ancarani, G. Gasaneo, and E. L. Gaggioli, Phys. Rev. A **92**, 042704 (2015).
[35] D. M. Wolkow, Z. Phys. **94**, 250 (1935).
[36] E. Chulkov, V. Silkin, and P. Echenique, Surf. Sci. **391**, L1217 (1997).
[37] T. Hecht, H. Winter, A. G. Borisov, J. P. Gauyacq, and A. K. Kazansky, Phys. Rev. Lett. **84**, 2517 (2000).
[38] H. Chakraborty, T. Niederhausen, and U. Thumm, Phys. Rev. A **70**, 052903 (2004).
[39] J. Zhao, N. Pontius, A. Winkelmann, V. Sametoglu, A. Kubo, A. G. Borisov, D. Sánchez-Portal, V. M. Silkin, E. V. Chulkov, P. M. Echenique *et al.*, Phys. Rev. B **78**, 085419 (2008).
[40] B. Obreshkov and U. Thumm, Phys. Rev. A **87**, 022903 (2013).
[41] Q. Liao and U. Thumm, Phys. Rev. A **89**, 033849 (2014).
[42] M. Ortuno and P. M. Echenique, Phys. Rev. B **34**, 5199 (1986).
[43] D. A. Papaconstantopoulos, *Handbook of the Band Structure of Elemental Solids* (Springer, New York, 2015).
[44] J. A. Knapp, F. J. Himpsel, and D. E. Eastman, Phys. Rev. B **19**, 4952 (1979).
[45] S. D. Kevan, Phys. Rev. Lett. **50**, 526 (1983).
[46] N. Zettili, *Quantum Mechanics, Concepts and Applications* (Wiley, Chichester, 2009).
[47] H. Friedrich and J. Trost, Phys. Rep. **397**, 359 (2004).
[48] C.-H. Zhang and U. Thumm, Phys. Rev. A **80**, 032902 (2009).
[49] J. J. Mortensen, L. B. Hansen, and K. W. Jacobsen, Phys. Rev. B **71**, 035109 (2005).
[50] J. Enkovaara, C. Rostgaard, J. J. Mortensen, J. Chen, M. Dulak, L. Ferrighi, J. Gavnholt, C. Glinsvad, V. Haikola, H. A. Hansen *et al.*, J. Phys. Condens. Mat. **22**, 253202 (2010).
[51] J. P. Perdew, K. Burke, and M. Ernzerhof, Phys. Rev. Lett. **77**, 3865 (1996).
[52] A. G. Borisov, D. Sánchez-Portal, A. K. Kazansky, and P. M. Echenique, Phys. Rev. B **87**, 121110(R) (2013).
[53] M. Lucchini, A. Ludwig, L. Kasmi, L. Gallmann, and U. Keller, Opt. Express **23**, 8867 (2015).